Pion production: A probe for coherence in medium-energy heavy-ion collisions

J. Stachel, P. Braun-Munzinger, R. H. Freifelder,* P. Paul, S. Sen, P. DeYoung,† and P. H. Zhang‡
Department of Physics, State University of New York at Stony Brook, Stony Brook, New York 11794

T. C. Awes, F. E. Obenshain, F. Plasil, and G. R. Young
Physics Division, Oak Ridge National Laboratory, Oak Ridge, Tennessee 37831

R. Fox and R. Ronningen
National Superconducting Cyclotron Laboratory, Michigan State University, East Lansing, Michigan 48824

(Received 19 November 1985)

The production of neutral pions has been studied in reactions of 35 MeV/nucleon $^{14}N+^{27}Al,Ni,W$ and 25 MeV/nucleon $^{16}O+^{27}Al,Ni$. Inclusive pion differential distributions $d\sigma/dT_\pi$, $d\sigma/d\Omega$, $d\sigma/dy$, $d\sigma/dp_\perp$, and $d^2\sigma/dy\,dp_\perp$ have been measured by detecting the two pion-decay γ rays in a setup of 20 lead glass Čerenkov detector telescopes. Special care was taken to understand and suppress background events. Effects of pion reabsorption are discussed and it is found that the cross sections presented here are substantially affected by such final state interactions. The comparatively large experimental cross sections and the shape of the spectral distributions cannot be accounted for in single nucleon-nucleon collision or statistical models; they rather call for a coherent pion production mechanism.

I. INTRODUCTION

To produce pions in nucleon-nucleon collisions, beam energies of at least 280 MeV are required. However, it has been known for a long time that in nucleus-nucleus collisions pions can be created at energies per nucleon significantly lower than this free nucleon-nucleon threshold. This has been understood[1] in terms of coupling the bound nucleon Fermi momenta to the momentum of relative motion of the colliding nuclei. Available data range from the first pion production in the laboratory[2] with 300–380 MeV α particles to more recent experiments[3] of π^+/π^- production with ^{12}C beams of energies as low as 60 MeV/nucleon.

Such a "Fermi momentum boosted" mechanism is not expected to work for arbitrarily low beam energies per nucleon, so that one might hope by studying pion production near the absolute threshold to learn about collective effects in nucleus-nucleus collisions. More quantitatively, using this single nucleon-nucleon collision model, Bertsch predicted[4] an effective threshold of about 54 MeV/nucleon. Furthermore, it was found[4] that this threshold is due not to the lack of high momentum components in the nuclei but to the decreasing phase space in the exit channel as the beam energy is lowered. We therefore aimed at experiments significantly below this 54 MeV/nucleon threshold. In the data presented here we used $E_{\rm lab}/A=35$ and 25 MeV since at such low beam energies a major fraction (40–100%) of the total center of mass energy is required to produce a pion. While light particle (p,d,t) spectra and also low energy γ spectra ($E_\gamma \lesssim 20$ MeV) reveal the statistical aspects of heavy ion collisions at these energies[5] and can usually be described in terms of temperatures, level densities, etc., the process we will discuss here requires the transformation of the majority or even all of the projectile's kinetic energy into just one new degree of freedom. One therefore can expect that the study of such a process should reveal the coherent aspects of medium energy heavy ion collisions, if there are such.

The experiments presented here concentrate on the measurement of inclusive production cross sections for neutral pions. This has several advantages over the measurement of charged pions: (i) Relatively large solid angles (5–10% of 4π) can be covered easily. (ii) The spectral distributions are not hampered by Coulomb distortion effects due to refocusing of the exiting pions in the Coulomb field of the remaining fragments. (iii) While the measurements of low kinetic energy charged pions is complicated by decay in flight, π^0 spectra can be measured with no low energy cutoff. This is particularly important as the bulk of the cross section is found at low pion kinetic energies (around 15–20 MeV).

In the following section we will give a description of the experimental technique and data analysis. In Sec. III the resulting integrated cross sections and differential pion distributions will be presented. First information about the 35 MeV/nucleon data has been presented already in a letter.[6] Here, we present data with much improved statistics (for the Ni target) and subjected to more sophisticated instrumental corrections due to our improved understanding of the response of and background events in the spectrometer. Part of the data discussed here has been presented in recent conference contributions.[7] The question to what extent the measured pion distributions are influenced by pion reabsorption in the surrounding nuclear matter and, therefore, have to be viewed as secondary distributions is addressed in Sec. IV.

In Sec. V the present data will be discussed in terms of and compared to predictions of various theoretical models. Simultaneous to our work there have been experiments on neutral pions with a similar experimental setup at somewhat higher beam energies[8,9] of $E_{lab}/A = 44-84$ MeV, and, very recently, at $E_{lab}/A = 20$ MeV.[10] Where relevant we will include results of these experiments in the discussion of the present data.

II. EXPERIMENTS

We report here information about three experiments measuring inclusive π^0 production cross sections using 35 MeV/nucleon ^{14}N beams of the $K=500$ superconducting cyclotron at Michigan State University (MSU) and 25 MeV/nucleon ^{16}O beams of the Holifield Heavy Ion Research Facility at Oak Ridge National Laboratory (ORNL). At 35 MeV/nucleon thick targets of natural Al, Ni, and W (62, 90, and 98 mg/cm^2) were bombarded for ≈ 50 h with an average beam intensity of 2 particle nA (experiment 1) and, in a more detailed investigation, the Ni target was exposed to 6 particle nA for ≈ 100 h (experiment 2). A 25 MeV/nucleon ^{16}O beam of 20–25 particle nA was used to bombard targets of natural Al and Ni (40 and 45 mg/cm^2) for also ≈ 100 h (experiment 3). The target thicknesses were chosen to optimize the integral pion yield versus energy loss of the beam in the target, which was about 10% of the beam energy for all beam-target combinations used. For an efficient random event suppression it was essential to use beams with 100% macroduty factor.

A. Measurement of neutral pions produced in heavy ion collisions

Neutral pions decay predominantly (98.8%) into two high energy γ rays on a time scale of 8.3×10^{-17} s, i.e., while still in the target. These two γ rays were detected in coincidence in a setup of lead glass Čerenkov detector telescopes arranged in various geometries. As an example in Fig. 1 the setup as used in experiment 2 is shown. It consisted of 20 lead glass telescopes each 49 cm distant (center of the converter, see below) from the target corresponding to a total solid angle of 6% of 4π. As depicted in Fig. 1 each telescope consists of a 1.6 radiation lengths or 5 cm deep converter section (front face 9.5×9.5 cm^2) of $F2$ glass, where the high energy γ ray is converted into an electromagnetic shower. The shower is then contained in the 15 radiation lengths (35 cm) deep absorber section of the respective telescope ($SF5$ glass, front face area 14.7×14.7 cm^2). The dimensions of the counters were chosen such that any electromagnetic shower originating there is fully contained, both laterally and longitudinally, in the absorber detectors. In experiment 1 the same geometry was used, however, with only ten telescopes each 24.5 cm distant from the target and covering a total solid angle of 10.2% of 4π. For experiment 3, 20 telescopes were arranged in two symmetric conical planes viewing the target at angles of 11 deg above and below a central plane; the distance to the target was 38.4 cm corresponding to a solid angle coverage of 9.6% of 4π.

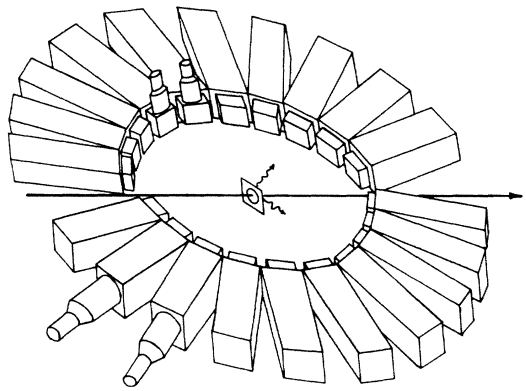

FIG. 1. Experimental setup to measure π^0 production in heavy ion collisions. The pion still in the target decays in two high energy γ rays; these are detected in a setup of lead-glass Čerenkov detector telescopes. The thick arrow marks the beam axis. The setup shown here was used in experiment 2. For details and dimensions see the text.

For a further suppression of cosmic ray background in experiment 3 the front face of each telescope was covered by a 2.5 cm thick plastic Čerenkov radiator[11] with front face area of 12.5 cm$\times$12.5 cm. Because of the 48 cm radiation length of this material less than 10% of the valid two-photon events are rejected by vetoing on events where any plastic detector in front of a lead glass telescope fired. For those events with at least two complete telescopes (absorber and converter) firing in fast (30 ns) coincidence with each other and with a beam pulse, all corresponding time and pulse height signals were recorded on magnetic tape.

B. Data analysis

The total γ energies for each event are obtained by summing up the energies deposited in the converter and absorber sections of the respective telescopes. The converter and absorber energy thresholds were 5 and 8 MeV, respectively, corresponding to an effective threshold of 13 MeV for each γ ray. An energy calibration was obtained from the signals of cosmic ray muons required to traverse the Čerenkov counters through their short sides. Following the procedures of Ref. 12, this corresponds to about 48 and 140 MeV deposited by an electromagnetic shower in converter and absorber, respectively. The γ-ray energy resolution for $E_\gamma \geq 50$ MeV typically follows a $10\%/\sqrt{E_\gamma(\text{GeV})}$ dependence. Both resolution and calibration were confirmed by test runs with 125 MeV electrons and 20–120 MeV tagged photons.[13] The γ angles θ_γ are defined by the converter positions with uncertainties, given by the respective opening angles, of $\Delta\theta_\gamma = \pm10$, ±5.5, and $\pm7°$ for experiments 1–3, respectively.

The time resolution of the Čerenkov counters was 1.4 ns (FWHM) for $E_\gamma > 20$ MeV. Events of true multiplicity 2 are defined by narrow time windows on absorber-absorber (4 ns), absorber-converter (5 ns), and absorber-beam (8.5 or 1.6 ns, depending on the beam microstructure) coincidences. In experiment 3 it was required in addition that none of the 20 plastic paddles fired.

Among the recorded events neutral pions can be identified by a peak in the invariant mass distribution

TABLE I. Geometric efficiency ϵ_g (%).

T_π (MeV)	θ_π (deg) 0–20	40–60	80–100
0–10	2.31	0.80	0.59
40–50	0.94	0.21	0.16
90–100	0.75	0.20	0.14

$$m_{\text{inv}}c^2 = 2\sqrt{E_{\gamma_1}E_{\gamma_2}}\sin(\phi/2) \quad (1)$$

about the π^0 rest mass of 135 MeV. $E_{\gamma 1}$ and $E_{\gamma 2}$ are the energies of the two γ rays and ϕ is their relative opening angle in the laboratory. The pion decay events are clustered about an opening angle

$$\phi_{\min} = 2\cos^{-1}(\beta_\pi) \quad (2)$$

corresponding to the symmetric decay; e.g., for a pion with kinetic energy $T_\pi = 100$ MeV this minimum opening angle is $\phi_{\min} = 70°$. All larger opening angles are allowed kinematically; however, their probability decreases steeply with increasing ϕ.

Taking into account the pion decay kinematics the geometric efficiency ϵ_g, i.e., the probability that both pion decay γ rays actually hit two telescopes of the setup, has been obtained from Monte Carlo simulations for the different geometries. In general, this efficiency decreases with increasing pion kinetic energy T_π. The dependence on pion emission angle is symmetric about $\theta_\pi = 90°$ and ϵ_g also decreases rather steeply between $\theta_\pi = 0°$ and 90°. Typical numbers for the setup shown in Fig. 1 are presented in Table I.

The probability that a γ ray, after hitting the setup, indeed leads to a signal above threshold in the converter section, the so-called conversion efficiency ϵ_c, has been obtained from Monte Carlo simulations[14] using the EGS code. It vanishes at $E_\gamma = 5$ MeV, increases with increasing γ energy [ϵ_c (50 MeV) = 0.45], and levels off at 0.68 for $E_\gamma > 120$ MeV. Recent measurements[13] with 20–120 MeV tagged photons are in fair agreement with these simulated values. The efficiency of the veto paddles for cosmic ray tagging (used in experiment 3) was measured out of beam to be >90%. Off-line measurements of the cosmic ray background were made to allow for corrections on the in beam results. These corrections are largest for $T_\pi > 40$ MeV.

Figure 2 shows the experimental invariant mass distribution in the mass range 60–200 MeV as obtained for 35 MeV/nucleon ^{14}N + Ni. This distribution corresponds to a total of about 900 pions and was obtained by applying all the above mentioned coincidence time gates and, for further background suppression, a cut eliminating events with $\phi < 70°$ and with $E_{\gamma 1}$ ($E_{\gamma 2}$) < 40 MeV. Efficiency loss due to these cuts was computed by Monte Carlo simulation and is discussed below.

There are two principal sources of background in the present experiments:

(i) beam correlated background. The main γ-ray background stems from nuclear deexcitation. Assuming a geometric cross section of 2 b for N + Ni, a mean γ-ray multiplicity of 25, and a π^0 production cross section of ≈ 100 nb (see below) with an associated γ multiplicity of 2, it is found that only 4×10^{-9} of the photons present are due to a π^0 decay. However, as the nuclear deexcitation γ rays are peaked around 1 MeV they are heavily suppressed by the absorber-converter thresholds and only piling-up several of them in one telescope will generate a signal at all. For the geometry shown in Fig. 1 the probability to have five of these photons hit one telescope is $\approx 10^{-6}$ and it is obvious that requiring a coincident signal in two telescopes strongly suppresses this background. At a much lower rate there are also single high energy γ rays (>15 MeV) present in the investigated reactions; they are suppressed by the $E_\gamma > 40$ MeV threshold and the coincidence requirement. For electrons there is a Čerenkov threshold of $T_e > 130$ keV in lead glass, which eliminates triggering due to x rays and slow Compton electrons or photoelectrons. We find electrons not to be a serious background contribution in the present experiments. In the forward telescopes there is a sizable contribution from fast neutrons[13] ($T_n > 50$ MeV), which, however, can be rejected via their different time of flight relative to the γ rays. Beam correlated background events that pass the prompt coincidence requirement and γ-energy thresholds are concentrated at low invariant mass ($\ll 70$ MeV) and dominate at small ϕ which means they are singled out from the pion events by the cuts on m_{inv} and ϕ as quoted above.

(ii) Background due to cosmic radiation. Both cosmic ray muons penetrating the array directly and cosmic-ray hadron showers originating from the concrete ceiling and shielding contribute. They are, however, strongly suppressed by requiring a multiplicity of exactly 2, prompt beam coincidence, $\phi > 70°$, 70 MeV $\leq m_{\text{inv}}c^2 \leq 200$

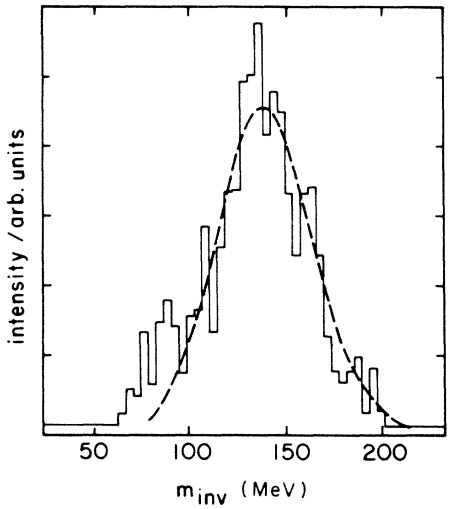

FIG. 2. Pion invariant mass spectrum measured for 35 MeV/nucleon ^{14}N + Ni after applying the various cuts discussed in the text. The intensity is in arbitrary units, the integral corresponds to a cross section of 115 nb or about 900 events. Also shown by the dashed line is the result of a Monte Carlo simulation.

MeV and for experiment 3 by the additional condition of the absence of any signal above threshold in the plastic veto counters.

Figure 2 shows, together with the histogram of the experimental data, the result of a Monte Carlo simulation for the invariant mass distribution. The calculation uses as input the experimentally observed T_π spectrum (see below) and includes the instrumental geometry and detector resolutions as well as all cuts applied to the experimental data. The good agreement of its shape with the data not only *a posteriori* justifies the treatment of these parameters but also demonstrates the effectiveness of the background suppression; remaining background contribution is indicated by the low energy tail of the experimental $m_{\rm inv}$ distribution. For experiments 1 and 2, the absorber-absorber coincidence resolution of 2 ns as compared to the ≈ 8 ns width of one beam bucket allows one to gate on random coincidences within the same beam bucket and thus enables an identification and quantitative subtraction of remaining background events (both beam correlated and cosmic), which amount to $\approx 18\%$ for experiment 2.

Having identified the π^0 decay events via their invariant mass, the total pion energy can now be calculated making use of the well known exact pion rest mass $m_\pi c^2 = 135.0$ MeV by the relation[15]

$$E_\pi^2 = \frac{2m_\pi^2 c^4}{(1-\cos\phi)\left[1-\left[\frac{E_{\gamma_1}-E_{\gamma_2}}{E_{\gamma_1}+E_{\gamma_2}}\right]^2\right]}, \tag{3}$$

from which the pion kinetic energy is obtained as

$$T_\pi = E_\pi - m_\pi c^2 . \tag{4}$$

The pion kinetic energy so determined is always positive and can be obtained fairly accurately[15] in spite of the relatively poor energy resolution (see above) of the lead glass counters. The pion emission angle in the laboratory is calculated from the measured γ energies and angles according to

$$\theta_\pi = \cos^{-1}\left[\frac{E_{\gamma_1}\cos\theta_{\gamma_1}+E_{\gamma_2}\cos\theta_{\gamma_2}}{(E_{\gamma_1}^2+E_{\gamma_2}^2+2E_{\gamma_1}E_{\gamma_2}\cos\phi)^{1/2}}\right] . \tag{5}$$

The respective resolutions are again obtained from Monte Carlo simulations and are typically (for the setup shown in Fig. 1) $\Delta T_\pi = 6$ and 30 MeV and $\Delta\theta_\pi = 25°$ and 8° for $T_\pi = 10$ and 100 MeV, respectively.

Knowing for each event the total pion energy and its emission angle, the pion momentum, its components $p_{||}$ and $p_\perp$, parallel and perpendicular to the beam direction and the rapidity

$$y = \tfrac{1}{2}\ln\left[\frac{E_\pi + p_{||}}{E_\pi - p_{||}}\right] , \tag{6}$$

can be determined with resolutions (determined by Monte Carlo simulations) of

$$\Delta p_\perp = 10\ (18)\ \text{MeV}/c \text{ for } p_\perp = 0\text{–}60\ (120\text{–}180)\ \text{MeV}/c ,$$

$$\Delta y = 0.07\ (0.05) \text{ for } p_\perp = 0\ (150)\ \text{MeV}/c ,$$

$$p_{||} = 0\text{–}60\ \text{MeV}/c ,$$

and

$$\Delta y = 0.04\ (0.03) \text{ for } p_\perp = 0\ (150)\ \text{MeV}/c ,$$

$$p_{||} = 120\text{–}180\ \text{MeV}/c .$$

From the measured double differential cross section $d^2\sigma/d\Omega\, dT_\pi$ the invariant cross section is obtained as

$$\sigma_{\rm inv} = E_\pi \frac{d^3\sigma}{dp^3} = \frac{1}{2\pi p_\perp}\frac{d^2\sigma}{dy\, dp_\perp} = \frac{1}{p}\frac{d^2\sigma}{d\Omega\, dT_\pi} \tag{7}$$

and the differential cross sections $d\sigma/dy$ or $d\sigma/dp_\perp$ result after integration over the respective other variable $(p_\perp, y)$.

All spectra and cross sections presented in the following had to be corrected for effects of the cuts in ϕ, $m_{\rm inv}$, and $E_{\gamma 1}$ and $E_{\gamma 2}$ applied to the raw data. These corrections are substantial. Whereas the *shape* of the angular distributions is not much affected the overall differential cross section scale and the kinetic energy spectrum receive sizable corrections for distortions. It can be seen easily where these corrections come from; the cut on $\phi > 70°$, e.g., affects pions decaying symmetrically for $T_\pi > 100$ MeV while the cut on low E_γ values rejects very asymmetric pion-decay events. However, we feel that these corrections can be handled accurately by (i) determination of the respective correction coefficients obtained by subjecting simulated data to the same analysis procedure as the experimental data; (ii) testing that after application of the necessary corrections the original distributions of simulated data are indeed regained. Typical corrections are of the order of 15% in $d\sigma/d\Omega$ for $T_\pi = 0$–20 MeV and 13 (60)% in $d\sigma/dT_\pi$ for $T_\pi = 10$ (100) MeV.

III. RESULTS

A. Kinetic energy distribution

Figure 3 displays the integrated pion kinetic energy spectrum for the ^{14}N + Ni reaction at 35 MeV/nucleon together with spectra obtained by gating on different regions of pion emission angles in the laboratory system. These spectra exhibit the typical behavior observed so far in all experiments on π^0 production at $E_{\rm lab} < 100$ MeV/nucleon: they are peaked at low kinetic energy ($T_\pi \approx 10$ MeV in this case) and fall off exponentially towards higher values of T_π. The solid lines in Fig. 3 are obtained by fitting the measured spectra for $T_\pi = 30$–100 MeV with the expression $d\sigma/dT_\pi = c\exp(-T_\pi/E_0)$. Independent of scattering angle we find a remarkably large inverse slope constant of $E_0 = 23 \pm 3$ MeV. This is in contrast to the trend observed at higher beam energies where slope constants determined in the same way were found to decrease[8] systematically from 27 to 22 MeV for the

$C + C \rightarrow \pi^0 + X$ reaction in the beam energy range of 84–60 MeV/nucleon. Similar results were obtained[8] in this beam energy range for asymmetric projectile target combinations such as $^{12}C + Ni$ or $^{12}C + U$.

The surprisingly large slope constant observed at 35 MeV/nucleon is not an isolated incident but rather shows up systematically in all data taken at 35 and 25 MeV/nucleon. In Fig. 4, e.g., we compare directly the spectrum obtained for $^{14}N + ^{27}Al \rightarrow \pi^0 + X$ with the result discussed above for $^{14}N + Ni$. The lines in these spectra are comparisons to various theoretical predictions as discussed in Sec. V. From this figure one can see that, within the experimental resolutions, both spectra have similar slope constants (the E_0 value obtained by fitting the $^{14}N + ^{27}Al$ data is $E_0 = 27 \pm 5$ MeV). E_0 values around 23 MeV are also required to fit $^{16}O + ^{27}Al \rightarrow \pi^0 + X$ and $^{16}O + Ni \rightarrow \pi^0 + X$ spectra at 25 MeV/nucleon.[16] As will be discussed below this leveling off in E_0 at low beam energies might be indicative for a change in pion production mechanism.

Also shown in Fig. 3 (dashed histograms) are spectra obtained by assuming a γ-energy independent conversion probability $\epsilon_c = 0.7$ for the setup. This is shown merely to demonstrate the maximum systematic uncertainty introduced by the calculated response. The similarity of both histograms shows the insensitivity of the deduced slope constants on uncertainties in the data reduction. The same conclusions also pertain for all other differential distributions as shown below.

While the overall slope of the kinetic energy spectra is found not to depend on the pion emission angle we note that there is a distinct excess of high energy ($T_\pi > 80$ MeV) pions at backward angles.

B. Angular distributions

The energy-integrated pion angular distribution for the $^{14}N + Ni$ system at 35 MeV/nucleon is shown in Fig. 5 together with distributions gated on different ranges of T_π. The surprising finding is that while the respective energy integrated distribution is forward-backward symmetric about 90° in the laboratory with a 0°/90° ratio of ≈ 1.5, the shape changes with increasing pion kinetic energy T_π. For the highest energy bin there is even a distinct backward rise of the cross section in the laboratory frame. Note that the binning in this spectrum is much finer than the experimental resolution (see above) so that

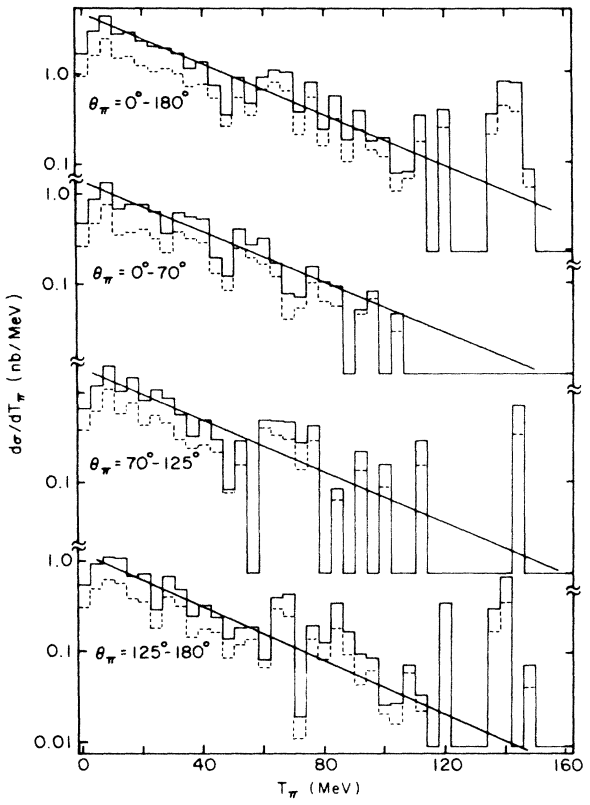

FIG. 3. Pion kinetic energy spectrum (solid histogram) in the laboratory frame for 35 MeV/nucleon $^{14}N + Ni$ integrated over all pion emission angles θ_π (top) and for various θ_π bins. For the meaning of the dashed histograms see the text. The straight lines represent an exponential with an inverse slope constant of 23 MeV.

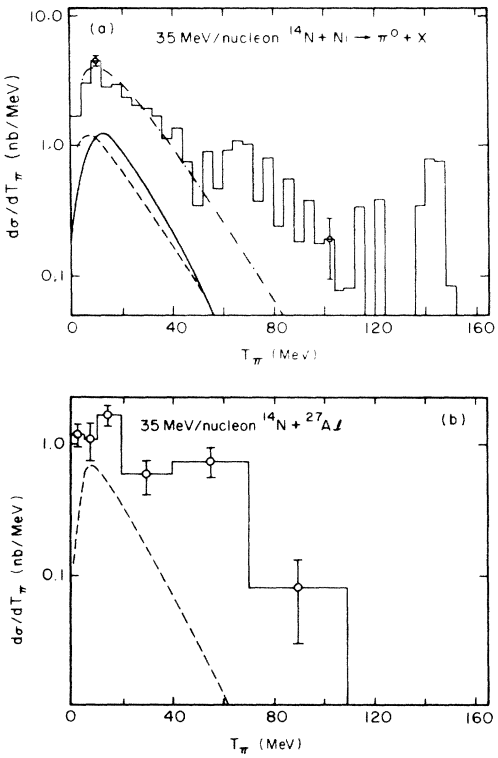

FIG. 4. Experimental pion kinetic energy spectra at 35 MeV/nucleon for the Ni and Al target. The spectrum for the Al target corresponds to the same measurements as shown in Ref. 6 but differs from the spectrum shown there by subtraction of the cosmic-ray background and use of the energy dependent conversion efficiency as discussed in the text (as compared to no cosmic subtraction and $\epsilon_c = 0.7$). The solid and dashed lines are predictions of Refs. 27 and 30, respectively. The dashed dotted line corresponds to a thermal spectrum (Ref. 20) with $T = 12.2$ MeV and is normalized to the data at low kinetic energies (10–60 MeV).

the bin to bin fluctuation is a direct measure of the statistical error in the data and shows the statistical significance of this result.

For the system $^{14}N + ^{27}Al$, however, we find a forward rise in the angular distribution [see Fig. 6(a)] with a maximum near $\theta_{lab}=50°$. Very similar behavior is observed as shown in the other panels of the same figure for ^{16}O induced reactions at 25 MeV/nucleon: Again the angular distribution for the ^{16}O + Ni system is clearly anisotropic with statistically significant maxima in the forward and backward hemisphere, whereas for $^{16}O + ^{27}Al$ it is forward rising with a maximum near $\theta_{lab}=40°$. Due to Lorentz transformation of the solid angle, angular distributions rising forward in the laboratory frame are expected for pion emission from a source moving in beam direction with forward-backward symmetric emission in the source's rest frame. Enhancements at large angles are difficult to explain in such models. All angular distribution measurements for symmetric projectile target combinations at higher beam energies[8,9] (44, 60, 74, and 84 MeV/nucleon) also exhibit a forward peaking in the laboratory. The Ni data at the lower beam energies presented in Figs. 5 and 6 are the only exception so far. It should be noted, however, that these are also the only angular distributions shown so far for a very asymmetric target-projectile combination. A possible explanation of this particular behavior in terms of reabsorption of the produced pions will be given in Sec. IV.

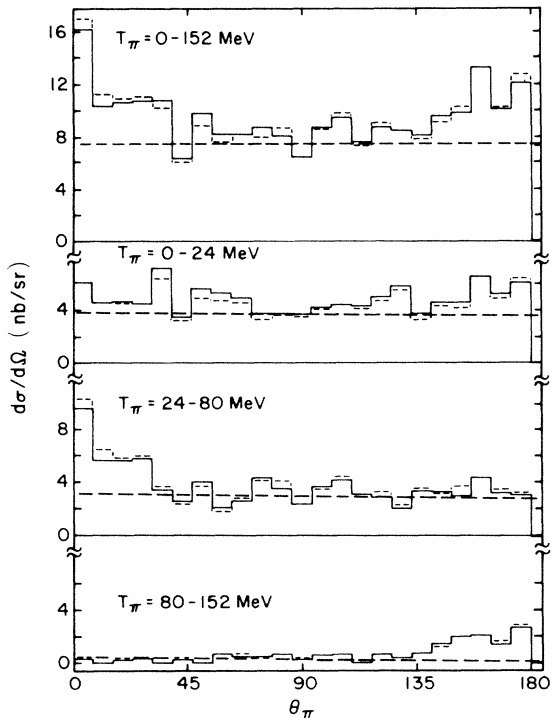

FIG. 5. Pion angular distribution in the laboratory frame for 35 MeV/nucleon ^{14}N+Ni integrated (top) over all pion kinetic energies and for different T_π bins (below). The thick dashed line corresponds to a constant $d\sigma/d\Omega$. It has been adjusted to the experimental values in the vicinity of $\theta_\pi=90°$ and is shown to better visualize the asymmetry of the data. For the dashed histograms see the text.

C. Invariant cross section

Figure 7 shows a two-dimensional plot of the invariant cross section versus rapidity and pion momentum perpendicular to the beam direction. In this scatter plot the size of the displayed points is proportional to the number of events N in the corresponding $p_\perp$, y bin ($\Delta p_\perp = 10$ MeV/c, $\Delta y = 0.05$) with a threshold at 0.015 nb c/(MeV unit rapidity). It is approximately symmetrically distributed about a centroid in rapidity of $\bar{y}=0.085\pm0.085$. Assuming pion emission from a single moving source this centroid would indicate the source velocity (rapidity). In the present case this source would be nearly at rest in the laboratory and clearly slower than one moving at half the projectile rapidity (indicated by $\frac{1}{2}p$ in Fig. 7). For the case of emission from a single moving source one would also expect the invariant cross section to be symmetric about the source velocity. To better illustrate possible small deviations from symmetry we show in Fig. 8 projections on the rapidity axis of the two-dimensional distribution integrated over all $p_\perp$ values as well as for selected $p_\perp$ ranges. The dashed line corresponds to the centroid of the rapidity distribution integrated over $p_\perp$; if computed for each $p_\perp$ slice individually, the centroid is found to move to slightly more negative values with increasing $p_\perp$ (it is $\bar{y}=-0.145$ for $p_\perp = 105$–250 MeV/c). From Fig. 8 it can be seen that these rapidity distributions are indeed asymmetric about the centroid; they all tail towards negative rapidities. This is particularly pronounced for the highest $p_\perp$ bin (105–250 MeV/c). It should be noted that these events in the negative rapidity tail are the very same that cause the backward rise in the angular distribution for the highest pion kinetic energies.

For later use, especially in the context of thermal models, we also project in Fig. 9 the invariant cross sections on the $p_\perp$ axis. The resulting transverse momentum distribution $d\sigma/dp_\perp$ has a maximum near $p_\perp \approx 50$ MeV/c for ^{14}N + Ni at 35 MeV/nucleon. Since all longitudinal (i.e., $p_{||}$) effects are integrated out in this distribution, it varies only little with system and beam energy.

D. Integrated π^0 production cross sections

To complete the information on the measurements we display in Fig. 10 the integrated cross sections for the different target nuclei. The resulting values are $\sigma_{\pi^0}=70\pm10$, 115 ± 13, and 159 ± 20 nb for inclusive π^0 production in reactions of 35 MeV/nucleon ^{14}N incident on ^{27}Al, Ni, and W targets. The errors given contain the statistical uncertainty, a 50% uncertainty of the background subtraction, and a 5% statistical uncertainty in the Monte Carlo results for the geometric detection efficiency. For 25 MeV/nucleon ^{16}O beams cross sections exist only for two targets and are not shown in Fig. 10. The integrated cross sections are 1.3 (±0.3) and 2.3 (±0.5) nb for the ^{27}Al and Ni target.

Also included in Fig. 10 are integrated cross sections measured at higher beam energies[8,9] with ^{12}C (84–60 MeV/nucleon) and ^{40}Ar (44 MeV/nucleon) projectiles. For all beam energies the measured cross section is increasing with increasing target mass number. At 84

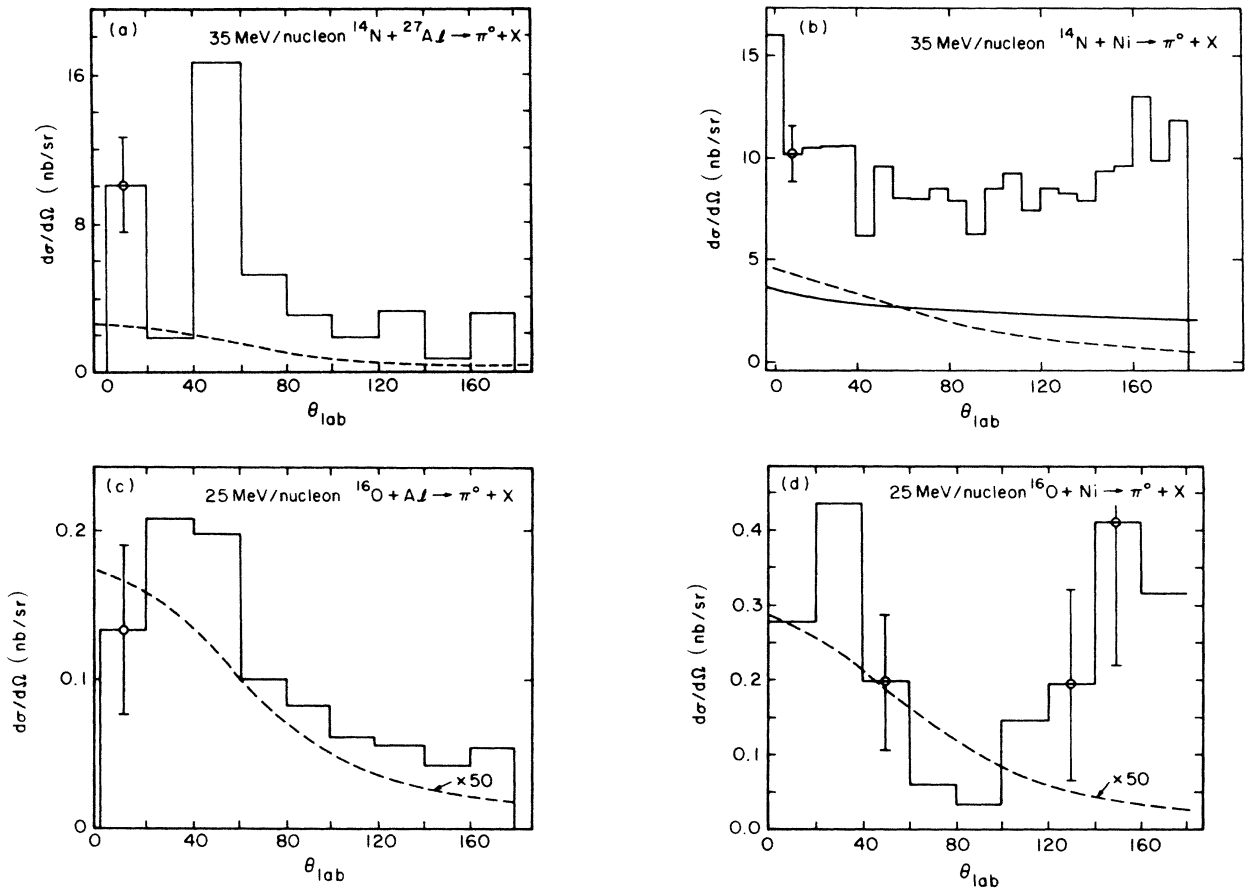

FIG. 6. Experimental pion angular distributions for the Al and Ni targets at beam energies of 35 MeV/nucleon [(a) and (b)] and 25 MeV/nucleon [(c) and (d)]. Typical experimental error bars are shown. The solid and dashed lines are predictions of Refs. 30 and 27, respectively. At 25 MeV/nucleon the calculations have been multiplied by a factor of 50 to show them on the same scale as the data.

MeV/nucleon this increase could be described[8] by an $A_T^{2/3}$ dependence (solid lines in Fig. 10), which would be expected if the pions are created by single nucleon-nucleon collisions. However, with decreasing beam energies we find increasing deviations from such an $A_T^{2/3}$ dependence and, in general, the experimental cross sections level off for very asymmetric target-projectile combinations. This could be interpreted in two ways.

(i) At lower beam energies pion production involves a more extended source than just two nucleons, e.g., the overlap volume between target and projectile nucleus. This would yield $\sigma\alpha(A_T^{1/3}A_P^{2/3}+A_T^{2/3}A_P^{1/3})$, which is sketched as the dashed dotted line at 35 MeV/nucleon in Fig. 10.

(ii) For larger target nuclei pion reabsorption effects increase.

Both possibilities will be discussed in more detail in the following.

IV. PION ABSORPTION

In the following we will discuss how far the present data could be influenced by pion reabsorption effects. Ex-

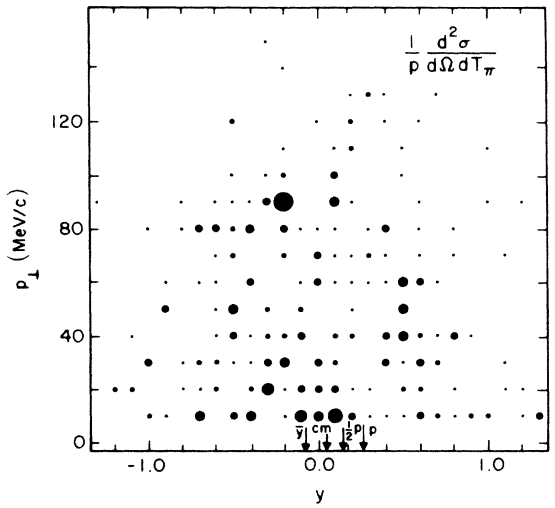

FIG. 7. Invariant pion production cross section at 35 MeV/nucleon $^{14}N + Ni$ as a function of the rapidity y and the momentum $p_\perp$ perpendicular to the beam direction. The size of the dots is proportional to the value of the double differential cross section with the integral corresponding to 115 nb. The different arrows on the rapidity axis mark the beam rapidity (p), half the beam rapidity ($\frac{1}{2}p$), the c.m. rapidity (c.m.), and the centroid of the experimental rapidity distribution $\bar{y}$.

perimental data for pion absorption cross sections are available[17] for π^+ and π^- induced reactions, but only for kinetic energies $T_\pi \geq 37$ MeV and, of course, only for ground state nuclear matter. The bulk of the data discussed here is at lower pion kinetic energies (see Figs. 4 and 5). To cover this pion kinetic energy range we, therefore, will use for the present discussion pion absorption mean free paths $\lambda_{abs}(T_\pi)$ as resulting from the optical model calculation of Hüfner and Thies[18] ($\Gamma_{abs}=120$ MeV), which reproduce reasonably well the experimental π absorption data for $T_\pi \geq 37$ MeV. In the energy range of interest here such calculations typically yield a maximum mean free path of $\lambda_{abs} \approx 3.6$ fm around $T_\pi = 25$ MeV. The λ_{abs} values decrease smoothly towards higher and lower kinetic energies to $\lambda_{abs}=3.0$ and 1.7 fm at 10 and 100 MeV, respectively. Similar but slightly smaller values are obtained in a recent relativistic calculation.[19] Comparing such mean free paths to the dimensions of the systems studied here, it is obvious that pion reabsorption cannot be neglected; the combined ^{14}N + Ni system, e.g., has a radius of ~ 7 fm at 50% density overlap.

To study effects of pion reabsorption on the present data in more detail we have performed Monte Carlo simulations based on $\lambda_{abs}(T_\pi)$ of Ref. 18. In these calculations a pion source of one nucleon mass (938 MeV) is assumed to move with kinetic energies between 1 and 20 MeV corresponding to $\beta=0.05$–0.20 along the beam direction. It emits pions isotropically in its rest frame with a Maxwell-Boltzmann kinetic energy distribution and a temperature varying between 5 and 20 MeV. This source is moving through cold nuclear matter, for instance through the combined N + Ni system with $A=72$, at dif-

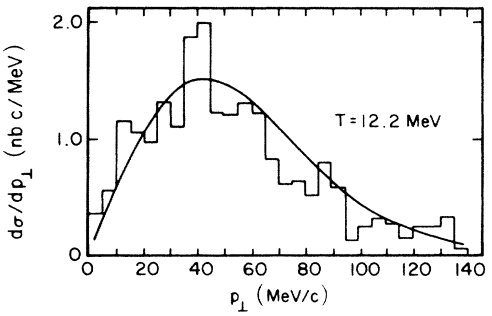

FIG. 9. Experimental pion perpendicular momentum distribution for 35 MeV/nucleon ^{14}N + Ni. Also shown is the theoretical distribution (solid line) for a thermal model (Ref. 20) where $d\sigma/dp_\perp \propto p_\perp \sqrt{T}\sqrt{m_\perp}\exp(-m_\perp/T)$ with $m_\perp=(m^2+p_\perp^2)^{1/2}$ and $T=12.2$ MeV.

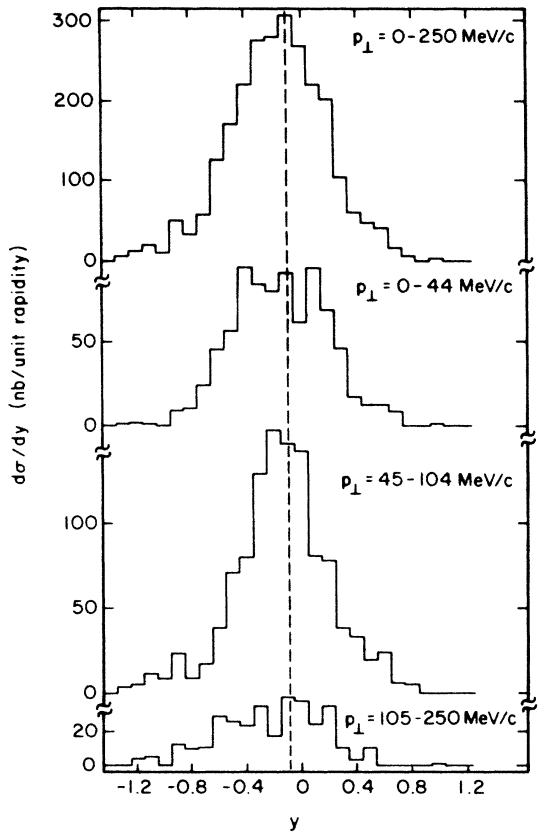

FIG. 8. Experimental pion rapidity distributions for 35 MeV/nucleon ^{14}N + Ni integrated over all values of the perpendicular pion momentum (top) and for three different $p_\perp$ bins. The dashed line corresponds to the experimental centroid for the top spectrum and is shown to visualize the asymmetry of the data about this centroid and the systematic downshift of the centroid with increasing $p_\perp$.

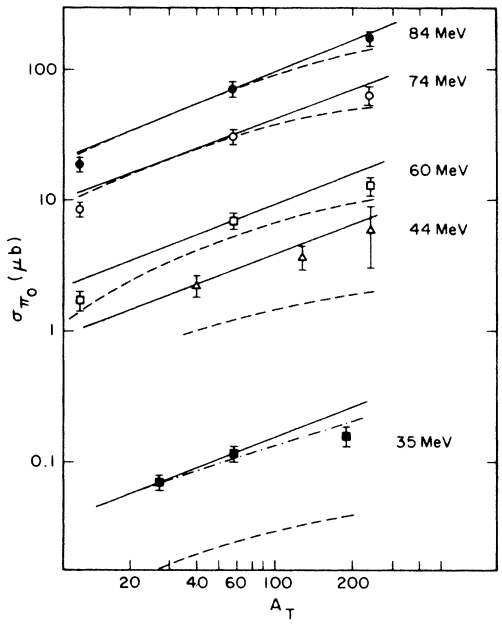

FIG. 10. Dependence of the integrated pion production cross sections from the target mass A_T for different projectile energies per nucleon. The respective projectiles were ^{14}N (35 MeV/nucleon), ^{40}Ar (44 MeV/nucleon, Ref. 9), and ^{12}C (60, 74, 84 MeV/nucleon, Ref. 8). The solid line corresponds to $\sigma \propto A_T^{2/3}$, the dashed-dotted line to $\sigma \propto (A_T^{2/3}A_P^{1/3} + A_T^{1/3}A_P^{2/3})$, and the dashed line results from the model calculation of Knoll and Shyam (Ref. 27).

ferent impact parameters b ranging from central to grazing collisions for the combined system. We investigate different impact parameters and source locations Z (for a precise definition see below) because (i) a nonzero average impact parameter would originate for a pion source smaller than the combined projectile plus target system after integration over all impact parameters. (ii) Stopping of the projectile before traversing the whole target nucleus (which is well conceivable but not proven at the beam energies discussed here) would lead to pion source location with $Z<0$. Here, and in the following, we use a coordinate system with the Z axis along the beam direction and $Z=0$ at the center of the combined projectile plus target system. In our simulations we always studied samples of 10^5 primary pions and obtained secondary (after reabsorption) distributions $d\sigma/dT_\pi$, $d\sigma/d\Omega$, $d\sigma/dp_\perp$, $d\sigma/dy$, and $\sigma_{\rm inv}(y,p_\perp)$ as a function of the source velocity and location. Note that while the initial position of the source is varied, we assume its lifetime τ to be so short that $\beta\tau \ll 1$ fm, i.e., $\tau \ll 10^{-22}$ s which seems reasonable for thermal models (see below). The temperature was chosen from a thermal model fit, following the prescription of Ref. 20, to experimentally observed pion perpendicular momentum spectra (see Fig. 9 and next section for details). For comparison we also studied the larger system of $^{14}N + {}^{194}Pt$ but in the following we will mostly concentrate on the $^{14}N + Ni$ system, for which the most detailed experimental information is available. The results are the following:

(i) For a pion source located at $Z=0$, $b=0$, i.e., in the center of the $A=72$ system, about 80% of the pions are absorbed; for a distance of $R=(Z^2+b^2)^{1/2}=4$ fm from the center this number goes down to 65%. This implies that the primary experimental cross section could be a factor 3–5 larger than what is observed.

(ii) Due to the fact that for $T_\pi > 30$ MeV the pion mean free path is decreasing with increasing T_π, pion absorption effects decrease the slope constant E_0 of the experimentally observed pion kinetic energy spectra. This effect strongly depends on the size of the system and the relative location of the source. A primary slope constant $E_0=25$ MeV decreases due to reabsorption to 16 MeV for a source in the center of the $^{14}N + Pt$ system, and to 23 MeV if the source is $R=3$ fm off the center. For the smaller $^{14}N + Ni$ system the corresponding secondary slope constants are 23 and 24 MeV for a source at $R=0$ and $R=3$ fm.

(iii) The pion angular distribution in the laboratory is strongly dependent on the source locations as is shown in Fig. 11 for a source velocity of $\beta=0.20$. The undisturbed distribution (middle of Fig. 11) corresponding to a pion source in the center of the combined $A=72$ system ($Z=0$, $b=0$) displays just the forward peaking due to the Lorentz transformation of an isotropic (in a frame moving with $\beta=0.20$) distribution into the laboratory system. The drastic effect on angular distributions of a source located at $Z=\pm 4$, $b=0$ fm is visible in the top and bottom there; pions going forward (top) and backward (bottom) can escape unhindered, whereas there is maximum absorption in the opposite direction. All distributions are normalized to yield the same integrated cross section. Of course, the exact shape of the measured angular distribution is determined by the interplay of primary angular distribution, source location, and the source velocity and for lower velocities and backward source location a distinct backward rise in $d\sigma/d\Omega$ can result. As the pion mean free path is changing with T_π so is the secondary angular distribution; in particular an increasing backward pion yield with increasing T_π is expected and found in the simulations for a backward located ($Z<0$) pion source. The gradual shape change of $d\sigma/d\Omega$ as a function of T_π depends, however, critically on the precise dependence of $\lambda_{\rm abs}$ on T_π.

(iv) We find that the shape of the calculated transverse momentum distribution $d\sigma/dp_\perp$ is basically not affected by pion reabsorption effects, which means that, within the thermal model of Ref. 20, the source temperature can be determined independently of other variables such as source location and velocity.

(v) The pion rapidity distribution, as expected, depends sensitively on the pion source velocity and its location. Our studies indicate that it is advantageous to analyze the shape of $d\sigma/dy$ rather than that of $d\sigma/d\Omega$ in order to get information on both source velocity and location. We find, in particular, that with decreasing source velocity the centroid of $d\sigma/dy$ is decreasing and approaching zero; as the pion source is moved backwards with respect to the beam direction ($Z<0$) again the centroid in $d\sigma/dy$ is decreasing (and can become even negative), but in this case the distribution is also becoming increasingly asymmetric. As displayed in Fig. 12 an analysis of the centroid of the rapidity distribution together with higher moments (skew-

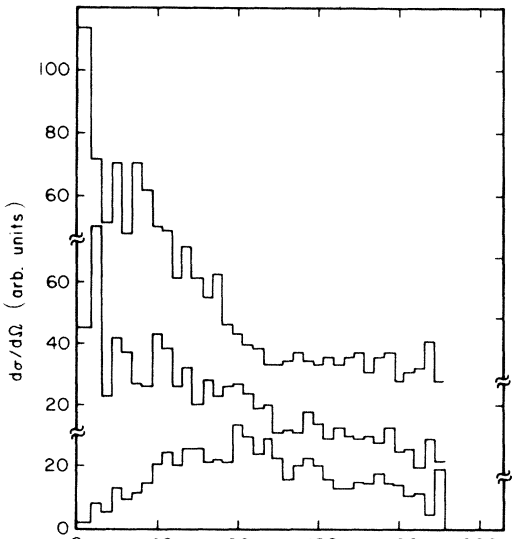

FIG. 11. The effect of pion reabsorption on the measured pion angular distribution (in the laboratory frame) for different source locations. The curves shown here result from Monte Carlo simulations and correspond to isotropic distributions in the rest frame of a source moving with $\beta=0.20$ and located at $Z=0$, $b=0$, i.e., in the center of the $^{14}N + Ni$ combined system (middle), at $Z=+4$ fm, $b=0$ (top), and at $Z=-4$ fm, $b=0$ (bottom). All three distributions are normalized to give the same integrated cross section.

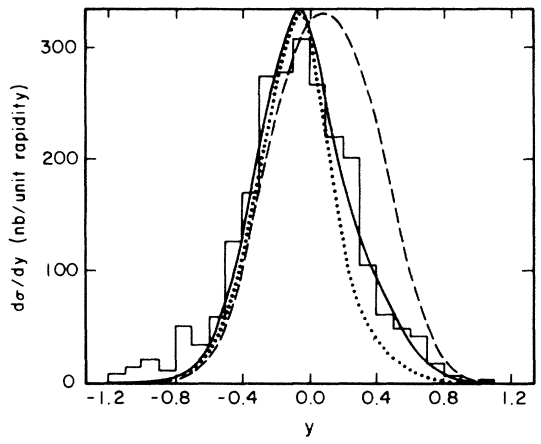

FIG. 12. Experimental pion rapidity distribution for 35 MeV/nucleon $^{14}N+Ni$ together with results of Monte Carlo simulations that include pion reabsorption and display the sensitivity of the experimental data to the primary source velocity. The curves correspond to $\beta=0.14$ (dashed curve), $\beta=0.09$ (solid curve), and $\beta=0.05$ (dotted curve). For the other parameters see the text.

ness or kurtosis) allows a determination of both source velocity and location (always assuming the simple picture of one source emitting pions thermally). The best agreement of the simulations with the 35 MeV/nucleon $^{14}N+Ni$ data is found for $\beta=0.09\pm0.03$ and $Z=-2.5\pm0.5$ fm. This reproduces rather well the experimentally observed $d\sigma/dy$ distributions and explains the shift towards negative values of y of the centroid of $d\sigma/dy$ and its increase in width with increasing perpendicular momentum (see Fig. 8). Such a location of the pion source is in accordance with recent simulations[21] of the collision dynamics of 25 MeV/nucleon $^{16}O+^{12}C$, according to which stopping of the projectile should occur in the overall center of mass system.

The conclusions for the present experimental data are the following: Measured[17] and calculated[18,19] mean free paths of pion absorption as well as the negative centroid of the experimental rapidity distribution, its asymmetry, the overall forward-backward symmetry of the pion angular distribution in the laboratory frame, and its backward rise at high kinetic energies observed in the present $^{14}N+Ni$ experimental data show the relevance of pion reabsorption for the experiments discussed here. In particular, one cannot conclude, as proposed recently,[22] from the similarity of observed π^+, π^0, and π^- production cross sections that effects of pion reabsorption are small. At the pion kinetic energies where the above comparison is made (i.e., $T_\pi \geq 150$ MeV) the absorption cross sections for π^+ and π^- (and hence also π^0) are similar and large.[17]

We have shown above how large the possible changes due to reabsorption are for the cross sections and the slope constants of the kinetic energy spectra; it is important to keep in mind for the following discussion that, if there is any change, both quantities would be even larger in the primary distributions than what we observe. The angular distribution is probably affected most and this may well explain the differences between our observations for the Al and the Ni target (see below and Fig. 6). We find, however, that the shape we observe for reactions induced by ^{14}N on the Ni target cannot arise from the effects of absorption on an isotropically (in the rest frame of the source) emitting source located at $Z<0$; the primary distribution has to be forward-backward peaked already (again in the source's rest frame). Then for the source location and velocity values estimated above, Lorentz contraction and forward absorption more or less cancel and could explain the observed $d\sigma/d\Omega$ spectra (Figs. 4 and 6). For the Al target stopping would probably occur closer to the center of the target and the system is smaller, i.e., absorption is less. This can explain the observed forward peaking in the angular distribution (Fig. 6) and is compatible with a primary (in the rest frame of the source) angular distribution which is identical for the two different targets.

Of course, we are aware that the present schematic Monte Carlo simulations cannot replace a full dynamic calculation; they should rather be viewed as an indication which experimental observables are sensitive to reabsorption effects and give a feeling for the size and direction of the changes between primary and secondary distributions (as given above). Ideally such effects should be included in the theoretical model calculation to be compared to the experimental data.

V. DISCUSSION

In order to bring the data of the present publication in perspective with existing pion production data measured at somewhat higher beam energies and for different target

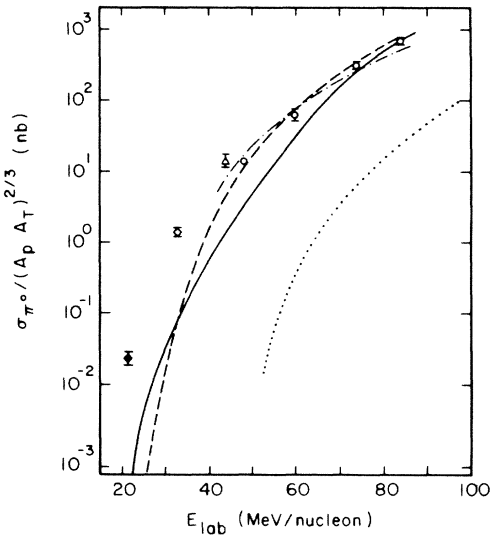

FIG. 13. Experimental integrated pion production cross sections divided by $(A_P A_T)^{2/3}$ for different beam energies. The different symbols signify $^{16}O+^{27}Al,Ni$ (closed diamond, present data), $^{14}N+^{27}Al,Ni,W$ (open diamond, present data), $^{40}Ar+^{40}Ca$ (open triangle, Ref. 9), and $^{12}C+^{12}C$ (open circles, Refs. 8 and 10). Also shown are results of a single nucleon-nucleon hard scattering model (Ref. 23) (dotted line), the extended phase space model (Ref. 27) (dashed line), a thermal model (Ref. 30) (solid line), and the bremsstrahlung model (Ref. 38) (dashed dotted line).

clusive pion production cross sections σ_{π^0} divided by $[A_T A_P]^{2/3}$ versus the beam energy per nucleon. Below the free nucleon-nucleon threshold for pion production, which is near 280 MeV in proton-proton collisions, cross sections are known to drop drastically. This is qualitatively in accordance with the more than four orders of magnitude reduction observed in σ_{π^0} between $E_{\text{lab}}=84$ and 25 MeV/nucleon as displayed in Fig. 13. However, as will be outlined in the following, a quantitative comparison with models considered so far shows that the experimental pion production cross sections are surprisingly large and, below 50 MeV/nucleon, still lack a quantitative description.

Before we discuss the various theoretical attempts to describe the present data, we review briefly the experimental features obtained so far in inclusive measurements of neutral pions produced at beam energies per nucleon less than 100 MeV:

(i) As a function of the target mass the cross sections increase, however, as discussed in Sec. IV, the cross sections shown in Fig. 10 are affected by reabsorption effects and have to be considered as lower limits. For the same reason the primary A_T dependence is expected to be steeper than what is shown in Fig. 10. Also, comparing the cross section[9] of 44 MeV/nucleon $^{40}\text{Ar}+{}^{40}\text{Ca}$ with that measured[10] for 48 MeV/nucleon $^{12}\text{C}+{}^{12}\text{C}$, the former one is found to be three times larger (after scaling with $A_P A_T)^{2/3}$, while reabsorption and the lower beam energy should lead to a reduced cross section if the scaling prescription is correct.

(ii) The inverse slope constants of the laboratory kinetic energy distributions (fitted to the data between 30 and 100 MeV) decrease between $E_{\text{lab}}=84$ and 60 MeV/nucleon from 28 to 23 MeV (spectra from Ref. 8) but then stay essentially constant (within the error bars) for all systems measured at 48, 35, and 25 MeV/nucleon as is shown in Fig. 14.

(iii) The angular distributions for 60–84 MeV/nucleon $^{12}\text{C}+{}^{12}\text{C}$ are forward-backward peaked in the center-of-mass frame.[8] The angular distributions for asymmetric systems at $E_{\text{lab}}/A=35$ and 25 MeV (as shown in Fig. 6) are affected by reabsorption (see Sec. IV). However, the observed shapes, in particular for the Ni target, cannot arise from isotropic distributions (in the c.m.) and require also a forward-backward peaking of the primary distributions.

(iv) If interpreted in terms of a single moving source, analysis of the invariant cross section for asymmetric systems as a function of rapidity and $p_\perp$ always yields a source velocity significantly slower than half the beam rapidity. In Sec. IV we have investigated for the system $^{14}\text{N}+\text{Ni}$ at E_{lab}/nucleon$=35$ MeV to what extent this might be caused by reabsorption effects; they are found to affect the apparent source velocity; however, even taking this into account, the data are inconsistent with emission from a source moving faster than $\beta\approx 0.1$. Smaller systems (e.g., N + Al, O + Al) should be affected less.

(v) As discussed in the previous section, the rapidity and angular distributions contain information about the average location of the source emitting the pions. The 35 MeV/nucleon $^{14}\text{N}+\text{Ni}$ data can be described consistently

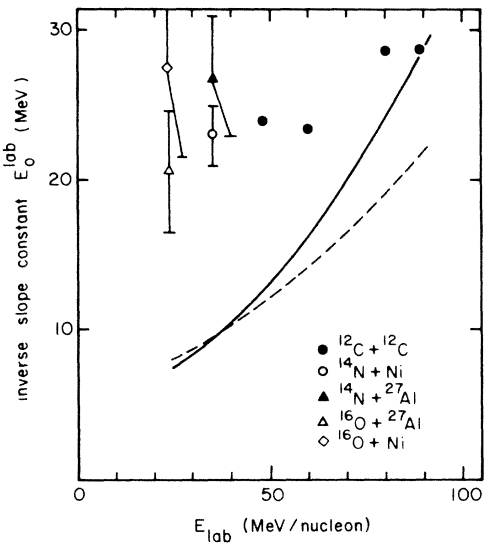

FIG. 14. Experimentally determined slope constants E_0 of pion kinetic energy spectra plotted as a function of beam energy/nucleon. For C + C spectra see Refs. 8 and 10. The solid and dashed lines correspond to predictions of Refs. 30 and 27, respectively. For details see the text.

if pions are emitted from a zone located about 2 fm backward from the center of the combined N + Ni system. The data for the other systems measured at $E_{\text{lab}}/A=35$ and 25 MeV are in qualitative agreement with this finding. However, statistics are too limited in these cases to allow a quantitative analysis of the pion source location.

A. Single nucleon-nucleon collisions model

In the following we will briefly discuss various models proposed to explain inclusive pion production data and compare their predictions to our measured data. The recent data on pion production at low beam energies triggered the reinvestigation of an idea dating back to a suggestion by McMillan and and Teller:[1] at beam energies below 280 MeV/nucleon pions can still be produced in single nucleon-nucleon collisions by taking into account the respective intrinsic nucleon momenta. Such an approach leads to a moderately successful description of inclusive production in proton-nucleus collisions and also nucleus-nucleus collisions down to roughly E_{lab}/nucleon$=100$–150 MeV if some kind of mean field, in the form of the real part of the ion-ion optical potential,[23] is included. However, the model fails completely at the lowest beam energies. Note that, in a pure Fermi-gas model, exclusion of final state phase space determines a threshold for this pion production mechanism at a relative momentum of $p=1.18p_F$ corresponding to $E/A\approx 54$ MeV and the predicted cross sections fall drastically as this limit is approached.[4]

Furthermore, in a recent publication,[24] it was argued that one should rather use the shell model for an improved initial state energy prescription. This puts much more restrictive limits on the energy range where such a single nucleon-nucleon collision mechanism is contribut-

ing significantly. At 84 MeV/nucleon the calculated cross section already underpredicts the data by more than a factor of 100; this calculation used a momentum distribution in accordance with measured (γ,p) data up to 500 MeV/c and did not even include Pauli blocking and reabsorption effects, which would reduce the calculated cross section by at least another order of magnitude.[24] These discrepancies will increase drastically at even lower beam energies.

Similar conclusions arise from the recent study by Guet and Prakash,[23] who investigated a single nucleon-nucleon hard collision process for pion production, where the two scattering nucleons are unbound in the final state (thus avoiding problems with Pauli blocking). The result is that calculations based on such a mechanism predict significant cross sections for laboratory energies in excess of 150 MeV/nucleon, while at lower beam energies and in particular for the energy range considered in the present publication ($E_{\rm lab}$/nucleon <50 MeV) the predicted cross sections are much too low compared to the experimental data (see Fig. 13). The calculation shown there (dotted line) even included an enhancement due to the attractive ion-ion optical potential ($U=100$ MeV). It merges with the experimental data at $E_{\rm lab}$/nucleon >150 MeV while at 50 MeV it already underpredicts the data by about four orders of magnitude. An explicit treatment of the distortion of the single particle wave functions during the collision in a time-dependent Hartree-Fock (TDHF) approach[25] yields an overall increase of only a factor of 2–3 as compared to predictions using time-independent momentum distributions. This is in accordance with the effect obtained by including the optical potential in the calculation of Ref. 23. In a more sophisticated model the collision dynamics is treated in TDHF by Tohyama *et al.*[26] However, calculations have only been performed so far for collisions of symmetric slabs at rather high energies of $E_{\rm c.m.}$/nucleon $=20$–40 MeV.

There are more experimental features that cannot be reconciled with such a single nucleon-nucleon collision mechanism.

(i) The inverse slope constants E_0 of pion kinetic energy spectra calculated within a single nucleon-nucleon collision mechanism are in general much smaller than experimental ones; Refs. 23 and 24 quote E_0 values about half as large as observed at $E_{\rm lab}$/nucleon $=85$ MeV. The fact that with decreasing beam energy the experimental E_0 values level off at a constant value of $E_0 \approx 23$ MeV is not compatible with a single nucleon-nucleon collision mechanism.

(ii) In a single nucleon-nucleon collision picture the source velocities are half of the beam rapidity, while the experimental average rapidities at $E_{\rm lab}$/nucleon <85 MeV/nucleon are significantly smaller even after corrections for absorption.

(iii) For integrated cross sections the single nucleon-nucleon collision picture predicts an $A_T^{2/3}$ dependence. While, in general, one has to be careful when comparing this quantity to experimental data because of reabsorption effects (see Sec. IV), the above example of 44 MeV/nucleon ^{40}Ar + ^{40}Ca vs 48 MeV/nucleon ^{12}C + ^{12}C is certainly in contradiction to an $A_T^{2/3}$ dependence.

B. Cooperative mechanisms

The single nucleon-nucleon picture for pion production evidently fails at the beam energies per nucleon considered here. A logical extension of such an approach is a model that involves the cooperative action of several target and projectile nucleons to create a pion. A pooling of the kinetic energy of several nucleons can be formulated either in terms of a quantum mechanical multiple off-shell collision picture or in a thermal model. The former approach has been used by Shyam and Knoll.[27] In their description the interacting projectile and target nucleons form a "dynamical" cluster, which then decays without intermediate energy constraints, i.e., in the phase space limit. There are two parameters involved in these calculations: The effective nucleon-nucleon cross sections and the freeze-out density which determines the number of final states. They are adjusted once and kept constant for all calculated systems. The alternative, thermal description is an extension of the compound nucleus model for pion production, which was proposed by Aichelin and Bertsch[28] for C on C collisions. As their compound nucleus picture evidently fails for asymmetric projectile-target combinations (cf., e.g., the target mass dependence of the integrated cross sections) it has been proposed[29] that only part of the projectile and target nucleus form the pion source. Such an approach was worked out recently by Prakash *et al.*[30] without any adjustable parameters by combining the geometrical concepts of the fireball model[31] with the compound nucleus approach.[28]

Both models in fact are very similar in that the inclusive invariant cross section for pion production is written as an incoherent sum over contributions arising from the M and N participating nucleons of the projectile and target, respectively,

$$\sigma_{\pi^0}^{\rm inv}(\mathbf{p}_\pi)=\sum_{M,N}\sigma_{\rm form}(M,N)F_{\rm decay}(\mathbf{p}_\pi)\ . \tag{8}$$

Here $\sigma_{\rm form}$ describes the formation of the (hot) overlap zone and $F_{\rm decay}(\mathbf{p}_\pi)$ is the decay probability of the "fireball" into a pion of momentum $\mathbf{p}_\pi$. The formation cross sections are calculated either by extrapolating results of a three-dimensional cascade as done in Ref. 27 or by making use[30] of the firestreak prescription of Ref. 31. While this should yield nearly identical results, the approaches of Refs. 27 and 30 differ somewhat in the prescription used to calculate $F_{\rm decay}$. Shyam and Knoll calculate $F_{\rm decay}$ by "counting" with equal probability all states available to a particular fireball ($M+N$) including multibody final states or those comprising clusters of deuterons, tritons, etc. In Ref. 30, the decay of the hot zone is treated using Weisskopf's compound nucleus theory[32] with level densities calculated in the Fermi gas approximation and inverse cross sections taken from experimental data for true pion absorption.[17] Both approaches assume full stopping in the nucleon-nucleon c.m. frame but not in the overall c.m. frame, as is indicated by the shape of the measured rapidity and angular distributions.

These differences in detail notwithstanding the two approaches give the following, very similar results: Integrated π^0 production cross sections are reproduced fairly well

for beam energies $50 < E_{lab}$/nucleon < 85 MeV (see Fig. 13). Also at these beam energies calculated pion kinetic energy spectra for symmetric and asymmetric systems agree well with experiment. With decreasing beam energy there are, however, increasing discrepancies: The calculated cross sections drop much faster than the experimental ones, underpredicting the data by a factor of 4 at 35 MeV/nucleon and by more than a factor of 50 at 25 MeV/nucleon. As can be seen from Figs. 4 and 14 (solid and dashed lines corresponding to the predictions of Refs. 30 and 27, respectively) the calculated pion kinetic energy spectra are also much steeper than the experimental ones; calculated inverse slope constants of $E_0 = 11$ and 6 MeV for E_{lab}/nucleon $= 35$ and 25 MeV have to be compared to an experimental value of about 23 MeV. Pion angular distributions are in both models predicted to be isotropic in the source's rest frame, i.e., forward peaked in the laboratory frame; they do not show the experimentally observed forward-backward peaking. Larger integrated cross sections, although at the expense of even steeper slopes, can be obtained within the thermal model (for details see Ref. 30) if the pion absorption cross section is assumed to follow a $1/v_\pi$ dependence near $T_\pi = m_\pi v_\pi^2/2 \approx 0$ MeV.

It should be noted that in the thermal model, where these quantities have been calculated, both the source rapidity and the $p_\perp$ distribution, which in this model would only reflect the source temperature, agree remarkably well with the respective experimental values for all beam energies. As an example for 35 MeV/nucleon $^{14}N + Ni$ the model of Ref. 30 predicts an average source temperature of 12.2 MeV and this is exactly what would result from a fit of this quantity to the experimental $p_\perp$ spectrum (see Fig. 9). On the other hand, the same temperature together with the source velocity of $\beta = 0.1$ (both from the thermal model and the experimental rapidity distribution, cf. Fig. 12) should describe the kinetic energy spectrum; this, however, is not at all the case as can be seen from Fig. 4; to describe this spectrum the temperature would have to be 17.4 MeV. (Note that the source temperature is *not* equal to the inverse slope constant E_0 defined in Sec. III.) This discrepancy in predicted and measured slope constant, also observed at other beam energies, shows that probably at the very low beam energies discussed here temperature is not a useful concept anymore to describe pion production.

C. Collective or coherent models

Figure 15 shows pion kinetic energy spectra transformed in the center of mass systems and plotted as a function of the energy available in the center of mass after pion emission. This available energy equals the center of mass energy for the respective reaction, corrected for the Q value,[33] minus the pion rest mass and minus the pion kinetic energy. The zero on this scale labels the kinematical limit, where the pion carries away the total energy available in the center of mass system. It can be seen from Fig. 15 that, within our experimental resolution, the data at E_{lab}/nucleon $= 25$ MeV come quite close to this phase space limit. The other interesting feature

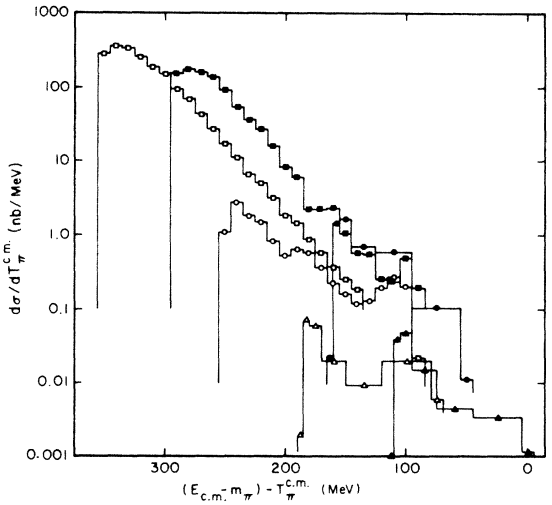

FIG. 15. Pion kinetic energy spectra as a function of the energy available in the c.m. system after pion emission. Experimental values are shown for 25 MeV/nucleon $^{16}O + {}^{27}Al,Ni$ (closed and open triangles, present data and Ref. 16), 35 MeV/nucleon $^{14}N + {}^{27}Al,Ni$ (closed and open dots, present data), 74 MeV/nucleon $^{12}C + {}^{12}C$ (closed squares, Ref. 8), and 84 MeV/nucleon $^{12}C + {}^{12}C$ (open squares, Ref. 8).

that can be seen in Fig. 15 is that as this kinematical limit is approached the data for different systems and different beam energies all merge together. Within the last 100 MeV of phase space the pion differential cross section scales with the full center of mass energy, while at higher values of the available energy it scales with the energy per nucleon or at most the kinetic energy of a few nucleons. Comparing, e.g., the kinetic energy spectra[8] at E_{lab}/nucleon $= 84$ and 74 MeV, one observes that they would match if shifted by 20 MeV, i.e., by approximately the difference in the kinetic energy of two projectile nucleons. It is evident from Fig. 15 that a shift by the full change of 60 MeV in $E_{c.m.}$ is too much and that is why the full squares lie above the open squares.

Near the limit of phase space the change in the total center of mass energy rather than the energy per nucleon seems to be the relevant quantity. Together with the failure of single nucleon-nucleon collision and cooperative or statistical models as discussed above this emphasizes the need for a fully coherent mechanism to describe the data presented here. Fully coherent mechanisms have been proposed by Klingenbeck *et al.*[34] to describe the "pionic fusion" data[35] measured for ^3He induced reactions at light target nuclei ($A_T \leq 10$). This model assumes Δ excitation which propagates in the compound nucleus and decays via pion emission to its ground state. It has, however, not been extended to heavier nuclei. Note that the thermal model of Ref. 30 discussed above can be extended to include the pionic fusion limit if a consistent Hauser-Feshbach description of formation and decay of the compound nucleus is employed. Another coherent mechanism has been proposed a few years ago by Brown and Deutchman[36] for a description of pion production in peripheral $^{12}C + {}^{12}C$ reactions. Here, a $\Delta(3,3)$ isobar is excited in

one C nucleus while the other one is excited to an $S=1$, $T=1$ state. Due to strongly decreasing form factors this mechanism would not work at the low beam energies discussed here. It can, however, be extended[37] to lower energies by using closure and thus including all possible target and projectile excitations; respective calculations are underway.[37]

Another collective approach is the bremsstrahlung model[38] proposed by Vasak *et al.*, which has been successfully applied for C + C collisions at higher beam energies of 44–84 MeV/nucleon[8,22] (see Fig. 13). In this model it is the sudden slowing down of the projectile (with a typical slowing down length of $\lambda \sim 1.5$ fm) that leads to pion emission. However, so far no calculations are available for the asymmetric systems as discussed here. Also, it is not easy to extend these calculations to our low beam energies as the model in its present formulation[38] does not contain any radiative energy loss; this approximation, while well justified to describe soft electromagnetic bremsstrahlung, is certainly not valid for the data discussed here, where a large fraction of the total center-of-mass energy is transformed into the creation of a pion.

VI. CONCLUSIONS

We conclude that production of neutral pions in heavy ion collisions has been observed at beam energies as low as 25 and 35 MeV/nucleon. In all cases the pions are identified by a clear peak around their invariant mass of 135 MeV. Detector response and data analysis have been modeled with Monte Carlo simulations; the agreement between simulated and experimental distributions is good. We made a special effort to understand and suppress both beam correlated and cosmic ray backgrounds. In spite of the small measured cross sections, the background subtraction from the differential pion distributions is less than 20% at an average and $<50\%$ even in the tails of the distributions. We find experimental evidence that the data are affected by pion reabsorption effects. Schematic Monte Carlo simulations, performed to model these effects, show which observables are altered and indicate the size of the effect. They also allow to extract information about the reaction dynamics from the data; in particular, we find a net backward location of the apparent pion source with respect to the projectile-target combined system implying full stopping in the overall center of mass system.

The experimental cross sections are surprisingly large and, in particular, the kinetic energy spectra extend to quite large energies. We observed pion production up to the kinematical limit, where the total center of mass energy is transformed into the production of one energetic pion and find that, towards this phase space limit, all kinetic energy spectra merge if plotted as a function of the energy available in the center of mass system. Single nucleon-nucleon collision models and also models that invoke the cooperative sharing of the beam energy of several projectile nucleons or statistical models fail at the low beam energies discussed here. The data, especially at the high pion kinetic energies, rather call for a coherent mechanism for pion production.

ACKNOWLEDGMENTS

We thank G. E. Brown, M. Prakash, and J. Knoll for stimulating discussions. Thanks are due to the staff of the National Superconducting Cyclotron laboratory at MSU and of the Holifield Heavy Ion Research Facility at ORNL for excellent support during the experiments. Financial support of the Alexander von Humboldt Stiftung, the National Science Foundation, and the U.S. Department of Energy (contract DEAC05-840R21400 with Martin Marietta Energy Systems) is gratefully acknowledged.

---

*Present address: Gesellschaft für Schwerionenforschung, Postfach 110541, 6100 Darmstadt 11, Federal Republic of Germany.

†Present address: Hope College, Holland, MI 49423.

‡Permanent address: Institute of Atomic Energy, Beijing, People's Republic of China.

[1]W. G. McMillan and E. Teller, Phys. Rev. **72**, 1 (1947); W. Horning and M. Weinstein, *ibid.* **72**, 251 (1947).

[2]E. Gardner and C. M. G. Lattes, Science **107**, 270 (1948).

[3]T. Johansson *et al.*, Phys. Rev. Lett. **48**, 732 (1982); V. Bernard *et al.*, Nucl. Phys. **A423**, 511 (1984).

[4]G. F. Bertsch, Phys. Rev. C **15**, 713 (1977).

[5]T. C. Awes *et al.*, Phys. Rev. C **25**, 2361 (1982); G. D. Westfall *et al.*, Phys. Lett. **116B**, 118 (1982); B. V. Jacak *et al.*, Phys. Rev. Lett. **51**, 1846 (1983).

[6]P. Braun-Munzinger *et al.*, Phys. Rev. Lett. **52**, 255 (1984).

[7]J. Stachel *et al.*, in Proceedings of the 1984 INS-RIKEN International Symposium Heavy Ion Physics, Mt. Fuji, J. Phys. Soc. Jpn. **54**, Suppl. II, 400 (1985); J. Stachel, Gesellschaft für Schwerionenforschung Report GSI-85-10, 1985, p. 155; in *Proceedings of the International Workshop on Gross Properties of Nuclei and Nuclear Excitations XIII, Hirschegg, 1985,* edited by H. Feldmeier (Technische Hochscule, Darmstadt, 1985), p. 1; in *Nuclear Structure 1985,* edited by R. Broglia, G. Hagemann, and B. Herskind (North-Holland, Amsterdam, 1985), p. 241.

[8]H. Noll *et al.*, Phys. Rev. Lett. **52**, 1284 (1984).

[9]H. Heckwolf *et al.*, Z. Phys. A **315**, 243 (1984).

[10]E. Grosse, in *Proceedings of the International Workshop on Gross Properties of Nuclei and Nuclear Excitations XIII, Hirschegg, 1985,* edited by H. Feldmeier (Technische Hochscule, Darmstadt, 1985), p. 65.

[11]Čerenkov plastic SCINTIPLEX I, manufactured by National Diagnostics, Somerville, N.J.

[12]J. S. Beale *et al.*, Nucl. Instrum. Methods **117**, 501 (1974).

[13]Detailed information on the response of the Pb glass Čerenkov telescopes to 20–120 MeV tagged photons and to neutrons will be published separately.

[14]C. Michel *et al.*, Nucl. Instrum. Methods (in press).

[15]H. W. Baer *et al.*, Nucl. Instrum Methods **180**, 445 (1981).

[16]First information about the 25 MeV/nucleon data is contained in a rapid communication, G. R. Young *et al.*, Phys. Rev. C

33, 742 (1986).
[17]K. Nakai *et al.*, Phys. Rev. Lett. **44**, 1446 (1980); D. Ashery *et al.*, Nucl. Phys. **A335**, 385 (1980); I. Navon *et al.*, Phys. Rev. C **28**, 2548 (1982).
[18]J. Hüfner and M. Thies, Phys. Rev. C **20**, 273 (1979).
[19]R. A. Mehrem, H. M. A. Radi, and J. O. Rasmussen, Phys. Rev. C **30**, 301 (1984).
[20]R. Hagedorn, Nuovo Cimento Suppl. III, 147 (1965).
[21]J. Aichelin and G. F. Bertsch, Phys. Rev. C **31**, 1730 (1985).
[22]E. Grosse, *Proceedings of the 5th Adriatic International Conference on Nuclear Physics, Hvar,* edited by N. Cindro, W. Greiner, and R. Čaplar (World-Scientific, Singapore, 1984), p. 347.
[23]C. Guet and M. Prakash, Nucl. Phys. **A428**, 119c (1984).
[24]R. Shyam and J. Knoll, Phys. Lett. **136B**, 221 (1984).
[25]W. Cassing, in *Proceedings of the International Workshop on Gross Properties of Nuclei and Nuclear Excitations XIII, Hirschegg, 1985,* edited by H. Feldmeier (Technische Hochscule, Darmstadt, 1985), p. 95.
[26]M. Tohyama *et al.*, in *Proceedings of the International Workshop on Gross Properties of Nuclei and Nuclear Excitations XIII, Hirschegg, 1985,* edited by H. Feldmeier (Technische Hochscule, Darmstadt, 1985), p. 13.
[27]R. Shyam and J. Knoll, Nucl. Phys. **A426**, 606 (1984).
[28]J. Aichelin and G. Bertsch, Phys. Lett. **138B**, 350 (1984).
[29]J. Aichelin, Phys. Rev. Lett. **52**, 2340 (1984).
[30]M. Prakash, P. Braun-Munzinger, and J. Stachel, Phys. Rev. C **33**, 937 (1986).
[31]G. D. Westfall *et al.*, Phys. Rev. Lett. **37**, 1202 (1976); J. Gosset *et al.*, Phys. Rev. C **16**, 629 (1977).
[32]V. Weisskopf, Phys. Rev. **52**, 295 (1937).
[33]A. H. Wapstra and G. Audi, Nucl. Phys. **A432**, 1 (1985).
[34]K. Klingenbeck *et al.*, Phys. Rev. Lett. **47**, 1655 (1981).
[35]N. Willis *et al.*, Phys. Lett. **136B**, 334 (1984), and references quoted there.
[36]G. E. Brown and P. A. Deutchman, Proceedings of the Workshop on High Resolution Heavy Ion Physics, Saclay, 1978, p. 212.
[37]M. Prakash, C. Guet, and G. E. Brown, Proceedings of the Second International Conference on Nucleus-Nucleus Collisions, Visby, Sweden, 1985, Nucl. Phys. **A447**, 626c (1986).
[38]D. Vasak, B. Mueller, and W. Greiner, Phys. Scr. **22**, 25 (1980); D. Vasak *et al.*, Nucl. Phys. **A428**, 291c (1984).